ORNL/TM-2019/1218

BTO 3.1.2.55 Milestone Report – Preliminary framework for heat exchanger flow distribution model

Viral K. Patel
Ayyoub Momen
Kashif Nawaz
Ahmad Abu-Heiba
Nathaniel O'Connor
Jamal S. Yagoobi

July 10, 2019

OAK RIDGE NATIONAL LABORATORY
MANAGED BY UT-BATTELLE FOR THE US DEPARTMENT OF ENERGY

ORNL/TM-2019/1218

Energy and Transportation Science Division

BTO 3.1.2.55 MILESTONE REPORT – PRELIMINARY FRAMEWORK FOR HEAT EXCHANGER FLOW DISTRIBUTION MODEL

Viral K. Patel[1]
Ayyoub Momen[1]
Kashif Nawaz[1]
Ahmad Abu-Heiba[1]
Nathaniel O'Connor[2]
Jamal S. Yagoobi[2]

1: Building Equipment Research Group, ORNL
2: Multi Scale Heat Transfer Laboratory, Worcester Polytechnic Institute, Worcester, MA

Date Published: July 10, 2019

Prepared by
OAK RIDGE NATIONAL LABORATORY
Oak Ridge, TN 37831-6283
managed by
UT-BATTELLE, LLC
for the
US DEPARTMENT OF ENERGY
under contract DE-AC05-00OR22725

CONTENTS

TABLE OF FIGURES

TABLE OF TABLES

NOMENCLATURE

ρ	density (kg/m^3)
u	fluid velocity (m/s)
F	body force (N/m^3)
p	pressure (Pa)
$\hat{p}_0$	outlet pressure (Pa)
n	surface normal (dimensionless)
$()^T$	transpose operator
∇	del operator
g	gravitational acceleration (m/s)
μ	dynamic viscosity (N s/m^2)
$\int_{d\Omega} d_{bc} dS$	surface integral
$\dot{m}$	mass flux (kg/s)
ϕ	phase parameter (dimensionless)
ϵ_{pf}	phase field interface thickness parameter (m)
ϵ_{ls}	level set interface thickness parameter (m)
γ	mobility parameter (m^3 s/kg)
χ	mobility tuning parameter (m s/kg)
θ_w	interface wall contact angle (radians)
ψ	phase field help variable (dimensionless)
λ	mixing energy density (N)
σ	surface tension coefficient (N/m)
β	slip length (m)
V	volume fraction (dimensionless)
u_{solid}	solid displacement (m)
S	stress (N/m^2)
S_{ad}	combined stress (N/m^2)
S_0	initial stress (N/m^2)
S_{ext}	external stress (N/m^2)
$(C{:}\varepsilon_{el})$	Cauchy stress tensor
C	stiffness tensor
E	Young's modulus (MPa)
ε	strain (dimensionless)
ν	Poisson's ratio (dimensionless)
ζ	bulk viscosity (Pa s)
v_a	acoustic velocity (m/s)
ρ_a	density perturbation (kg/m^3)
c_0	speed of sound (m/s

EXECUTIVE SUMMARY

This report summarizes the modeling effort for this project, which had an overall goal to provide insight and guidance in the design of the heat exchanger (HX) flow distribution control using piezoelectric transducers. Over the past three quarters, the following progress was made in terms of computational fluid dynamics modeling:

- Single-phase flow modeling of flow in HX header and microchannels:
  - This has involved flow of liquid through the HX in 2D and 3D, with parametric variation (for 2D cases) in mass flow rate and microchannel insertion depth.
  - Although this was an important first step in modeling, no flow maldistribution was observed (as expected) due to the incompressibility of liquids.

- Preliminary two-phase flow modeling:
  - Various methods have been explored including disperse methods for bubbly flow and those involving interface tracking such as level set and phase field.
  - The goal was not to solve the problem of two-phase flow, but rather focus on particular geometry and conditions which are relevant to the project at hand.
  - Along these lines, a pertinent example of the work in this report includes a study of interface motion at various times for a simulated air-pocket trapped in the HX header filled with water (analogous to ongoing experimental work).
  - The phase field simulation results allow us to calculate the effect of such two-phase flow conditions on the overall flow distribution, which is also being explored experimentally.

- Ultrasound modeling
  - Two methods of ultrasound modeling have been studied to determine how vibrating surfaces interact with fluid domains: acoustic streaming and fluid-structure interaction.
  - Using the results of this work, the expected vibration frequencies and amplitudes necessary to influence the fluid domain can be determined.
  - A pertinent example of the results generated include the velocity distribution in a liquid domain which has a structure vibrating at 25 kHz at the bottom, which show the formation of a “jet” emanating from the structure into the domain.
  - The data can be used to determine if appreciable pressure and flow can be generated in the fluid and, subsequently, what characteristics of piezoelectric transducers would be needed to experimentally control and alter the flow distribution.

The above preliminary results have laid the foundation for the modeling phase of the project, which will be continued as the project progresses. As more complexity is introduced into the models, the results will be used to supplement the upcoming experimental work. All of the results are summarized in this report.

1. INTRODUCTION

The goal of the modeling task is to provide insight and guidance into the design of the heat exchanger (HX) flow distribution control system. The models allow us to study different parameters which affect maldistribution, as well as the piezoelectric transducers which will be eventually used to mitigate that maldistribution. Modeling is performed in COMSOL Multiphysics 5.3a [1]. Initial single-phase flow models were developed to understand the effect of geometric parameters on the severity of maldistribution in the HX. Initially the entire HX was modeled, but as more complexity was introduced, the model was reduced to the inlet header only to save computational time.

Typical evaporators in HVAC systems do not have pure single-phase liquid at the inlet header, but rather a two-phase mixture. To study the effect of this two-phase flow condition, several different methods were explored on a simplified geometry such as bubble transport and interface tracking through the level-set and phase-field methods. Parallel benchtop experiments are being performed with an air-water mixture to supplement these models. Due to the complexity of modeling two-phase flow, the header geometry was reduced to a 2-D representation to save computation time in these preliminary models.

Modeling of acoustic streaming phenomenon is somewhat scarce in the literature. For the purpose of this project, two different approaches for modeling this phenomenon were explored. Time averaged pressure fields can be used to apply a body force term to laminar Navier-Stokes momentum equations to reasonably approximate the acoustic streaming phenomenon. In addition, fluid structure interaction through the Arbitrary Lagrangian Eulerian (ALE) method was used to directly simulate a vibrating surface to produce an acoustic streaming effect.

These models will be combined to accurately simulate the conditions of the header to determine the best way to control maldistribution in the benchtop experiment. The modeling effort will continue for the remainder of the project to refine our understanding of the underlying phenomenon and inform future decisions for the experimental work.

2. SINGLE-PHASE FLOW MODELING

Computational fluid dynamics (CFD) modeling of single-phase flow began with a simple model of liquid flowing through an evaporator, which consisted of a header with three microchannel tubes. For the sake of simplicity, it was decided early on to only model three tubes spaced in the center and extreme ends of the header, as these were thought to be sufficient to study refrigerant maldistribution while reducing computation time. Figure 1 illustrates the CFD domain of interest for these simulations.

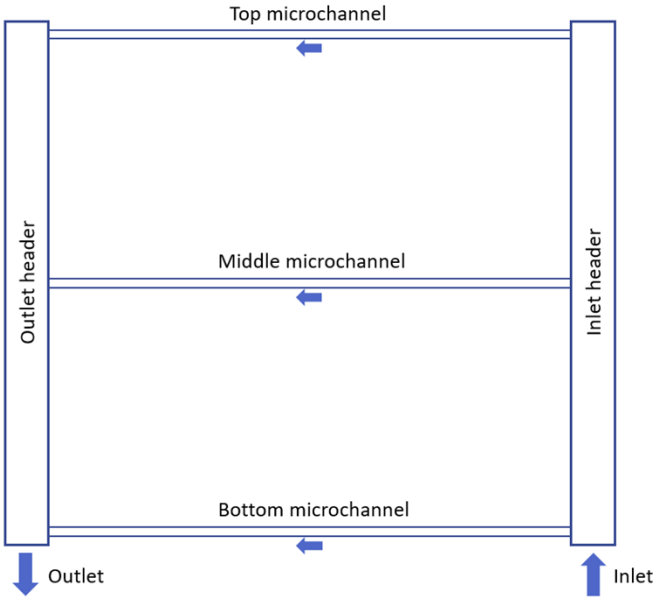

Figure 1. Illustration of CFD simulation domain for heat exchanger with three microchannels

2.1 HX WITH EQUIVALENT TUBE DIAMETER

For these initial models, a refrigerant-side mass flow rate of 0.01 kg/s was used as the inlet condition; this was calculated as a typical mass flow rate for an evaporator in a heat pump system with R-134a as the working fluid and a total capacity of 1.5 kW. A tube diameter of 3.5 mm was selected as an equivalent hydraulic diameter to the microchannels used in the benchtop experiment (see Section 2.2 for details on microchannel geometry). The height of the header was selected to be 305 mm (12 in) and the inlet diameter was selected to be 12.7 mm (0.5 in). The working fluid was selected to be water to maintain consistency with the benchtop experiment. Symmetry in the Y-Z plane was used to reduce the computation time.

The models were implemented into COMSOL using the laminar flow interface. The Navier-Stokes equations for continuity and momentum (Eqs. 1 and 2, respectively) for incompressible flow were solved:

$$\rho \nabla \cdot (u) = 0 \tag{1}$$

$$\rho(u \cdot \nabla)u = \nabla \cdot [-pI + \mu(\nabla u + (\nabla u)^T)] + F + \rho g \tag{2}$$

The initial conditions for the model were left at the default values of 0 in COMSOL for velocity and pressure. The material properties are taken from COMSOL's material library at a temperature of 20°C and pressure of 1 atm. The walls of the geometry were specified as no-slip boundary conditions as shown in Eq. 3.

$$u = 0 \tag{3}$$

The inlet mass flowrate was specified as a normal mass flow rate applied to the inlet surface shown in Eq. 4.

$$-\int_{d\Omega} \rho(u * n) d_{bc} dS = \dot{m} \tag{4}$$

The outlet was specified as 0 Pa gauge pressure applied at the outlet surface shown in Eq. 5.

$$[-pI + \mu(\nabla u + (\nabla u)^T]n = -\hat{p}_0 n \tag{5}$$

Gravity was also applied as a body force in the -z-direction across the entire domain. The mesh consisted of tetrahedral elements with boundary layers. The mesh is refined at the inlets and outlets of the tubes, resulting in a total of ~1.86 million elements. A stationary study was computed and is shown below in Figure 2 and Table 1.

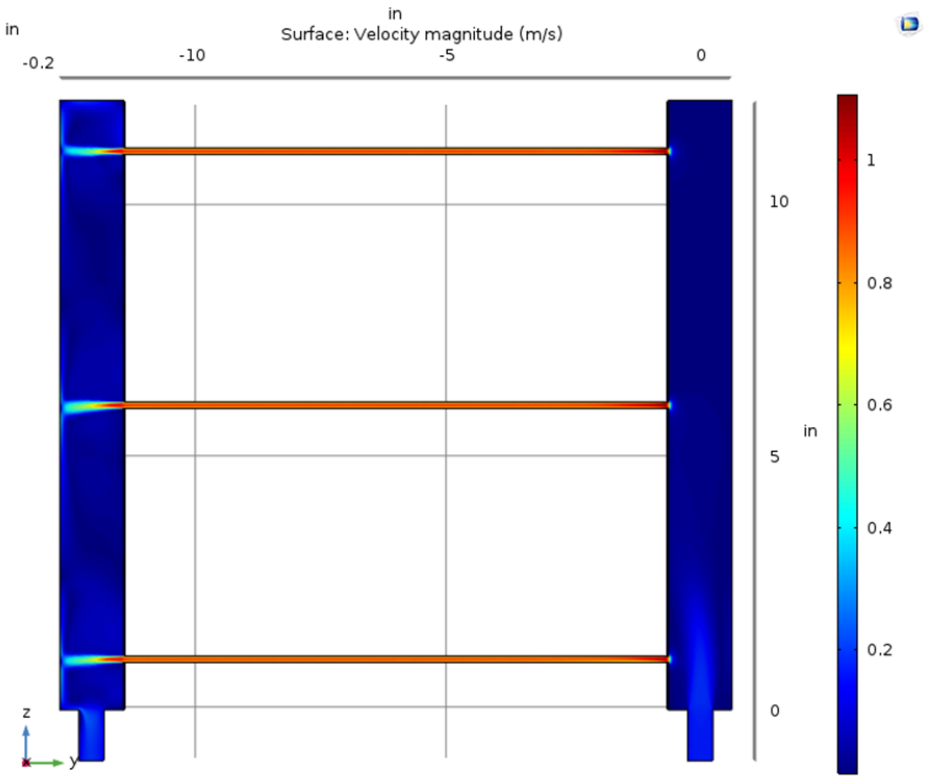

Figure 2. Initial single-phase flow model - velocity results (inlet at bottom right)

Table 1. Mass flow distribution for initial single-phase flow model results in Figure 2

Tube	Bottom	Middle	Top
% of total flow	33.0%	33.4%	33.5%

The single-phase flow results do not show a very substantial level of maldistribution. The difference in mass flow rates is on a scale similar to the numerical error of the simulation. The bottom tube likely has the lowest mass flow rate due to its proximity to the inlet.

2.2 HX WITH ACTUAL MICROCHANNEL GEOMETRY

Having developed this simplified single-phase model, complexities were slowly introduced to more accurately simulate the benchtop experiment. As it was decided that a microchannel evaporator would be the focus of this study, the three parallel tubes were replaced with microchannels, each containing five ports. The outer dimensions of the microchannel were 25.4 mm × 2.0 mm and the port dimensions were 0.9 mm × 4.5 mm. The length of the microchannels was 305 mm.

Implementation of the microchannel geometry into COMSOL is shown below in Figure 3. Symmetry across the y-z plane is taken advantage of to reduce computation time. The mesh must be refined at the inlet to the microchannel to properly capture the rapid acceleration of the fluid entering the channels. The mesh consists of a total of 4.57 million tetrahedral elements. Note that the microchannels as shown in Figure 3 are flush with the header and not inserted at all. The boundary conditions are similar to the previously stated case. A Neumann boundary condition is applied on the symmetry plane. An inlet mass flow rate of 0.005 kg/s is applied, and the outlet pressure is specified at 0 Pa gauge. The working fluid is water. Gravity is specified as a body force term. The velocity magnitude distribution results are shown below in Figure 4.

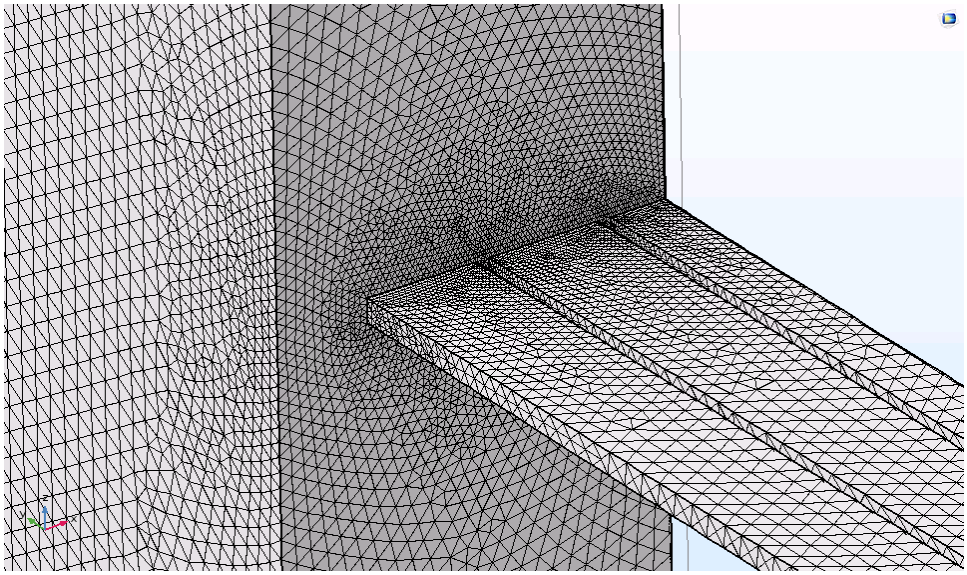

Figure 3. Microchannel geometry and mesh at transition from header

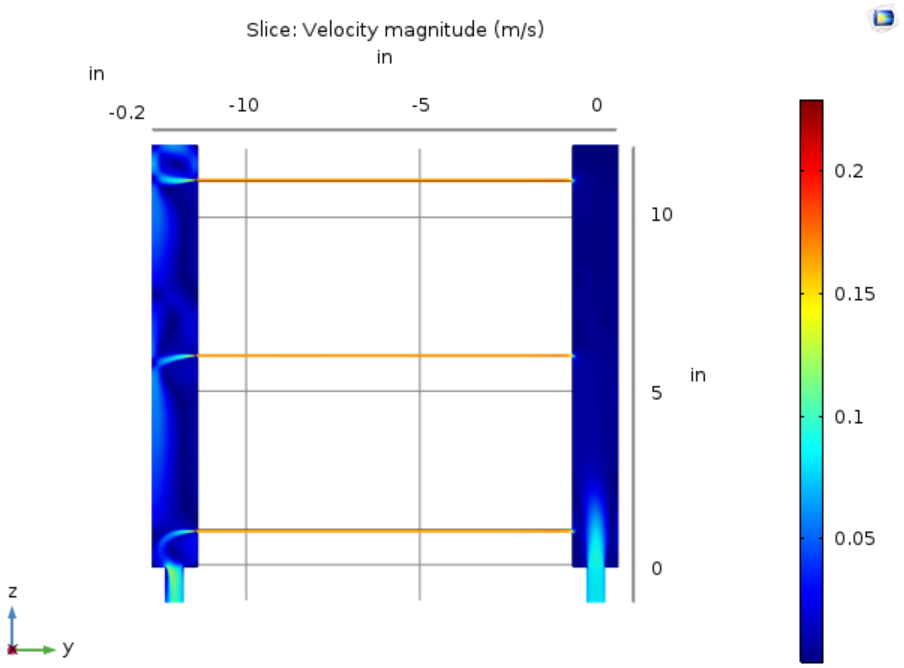

Figure 4. Single-phase flow model - velocity magnitude distribution for HX with microchannel geometry (inlet at bottom right)

Similar to the previous single tube model, minimal flow maldistribution was observed. The computation time for these models were about 24 hours. To accelerate solutions and results, the team decided to only simulate the inlet header of the evaporator. This was also justified because maldistribution is predominantly affected in the inlet header. Upstream flow control has been found to be more effective than downstream control [2]. The computation time could also be substantially reduced by eliminating over half the geometry and thus half the elements. Maldistribution upstream can also be implemented upstream through boundary conditions on the outlets of the header. Previously the header was oriented vertically, but the model was adjusted to be horizontal such that gravity would play a less important role. The outlet boundary conditions were specified at each individual channel to be 0 Pa gauge, or essentially open to atmosphere. This replicates the benchtop experiment in which the channels are inserted into a single header and open on the other end such that flowrate measurements are possible.

The goal of this model is to study the effect of microchannel insertion depth on flow distribution. It is expected that a microchannel inserted deeper into the header would experience a lower flowrate compared to the others. However, in pure single-phase flow, the difference in flowrate is miniscule. This is supported by both experimental results and the modeling results shown below. The 3D header geometry is shown below in Figure 5. In the geometry shown below, the first two microchannels are inserted 2.54 mm (0.1 in), while the last microchannel near the end of the header is inserted 9.525 mm (0.375 in). The depth of 9.525 mm is the maximum insertion depth for the initial header design in the experimental setup. Note that only the internal volume of the header and tubes is modelled. The channels are only modelled for 6.35 mm (0.25 in) of length as they reach a steady flow field rapidly. For this same reason, we can employ a swept mesh on the microchannels as shown in Figure 6. An extremely fine mesh is required near the inlets to the microchannel ports to properly capture the physics due to the high velocity gradients. There are a total of 3.63 million elements in this geometry, nearly double the original full exchanger single geometry even with symmetry, but less than the full exchanger microchannel geometry.

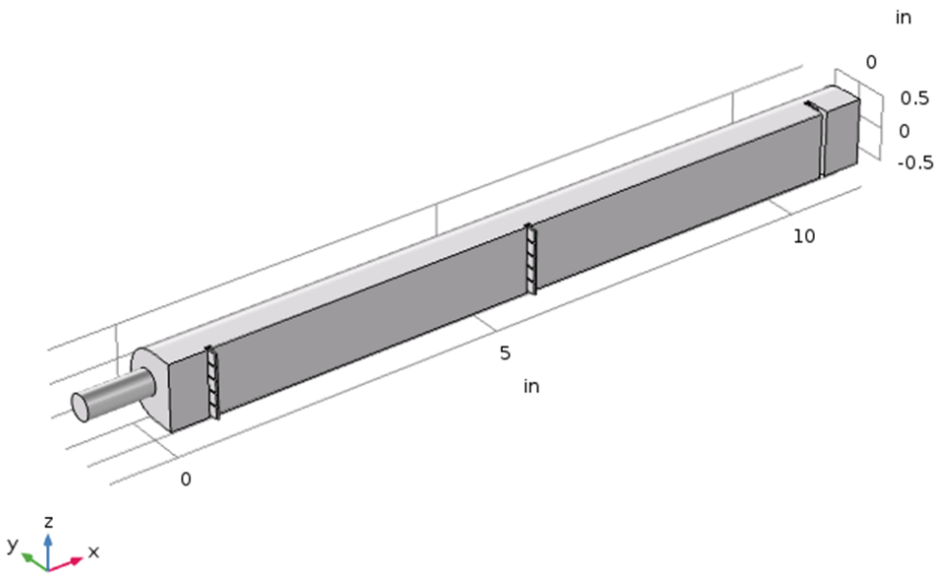

Figure 5. Horizontal header geometry with tube insertion

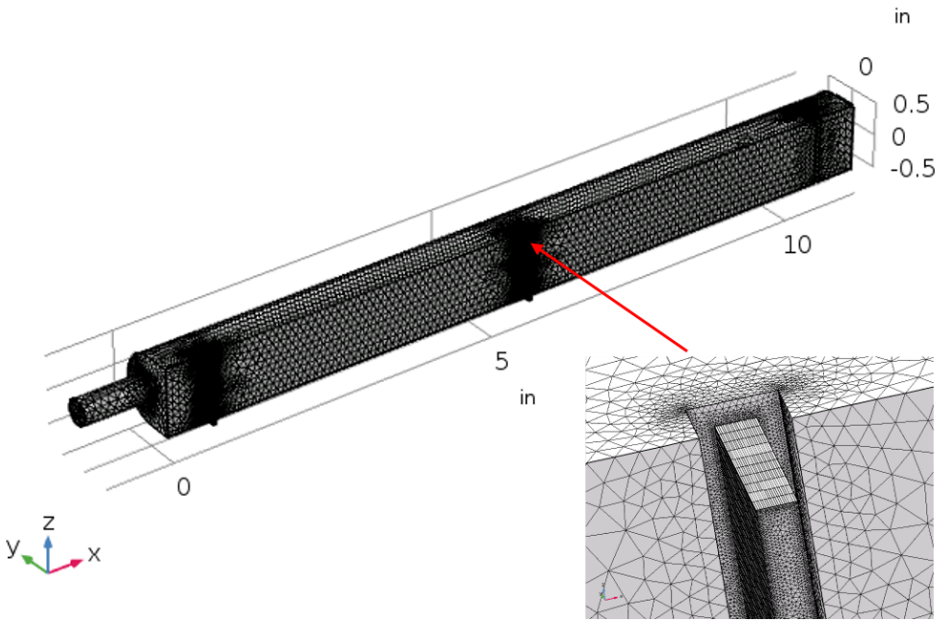

Figure 6. Horizontal header with microchannel insertion mesh - detail view showing swept mesh

While the single header model is less computationally expensive than the full exchanger, it is still a computationally intensive problem requiring many hours to solve. Additionally, in some cases of higher flowrate the solution is inherently time-dependent. Time dependent solutions were carried out until a sufficient “steady state” was reached. Introduction of time derivatives also adds another source of error to the numerical solutions. Since each 3D solution was taking approximately 12 hours, the model was moved to a 2D representation with a finer mesh in order to vary several parameters in a timely manner, as discussed in the next section.

2.3 HX WITH 2D HEADER GEOMETRY ONLY – PARAMETRIC STUDY

Our goal in this part of the study was the see if there was any substantial effect from varying insertion depth and flowrate. The 2D geometry is a top down view of the header. The boundary conditions are the same as the previous 3D case, however now the inlet mass flowrate is varied as a parameter between 0.005. 0.01, 0.025, and 0.05 kg/s. The insertion depth of the microchannels was also varied between 0-9.525 mm (0-0.375 in) at increments of 3.175 mm (0.125 in) for each microchannel. An insertion depth of 0 mm corresponds to the microchannel being flush with the header plate in the benchtop experiment. An insertion depth of 9.525 mm is the maximum insertion depth limited by the header geometry. An example of the velocity distribution results for all microchannels inserted 9.525 mm is shown below in Figure 7 and Figure 8. The model was solved with a parametric sweep, giving results for all combinations of insertion depths and flowrates, resulting in a total of 256 solutions.

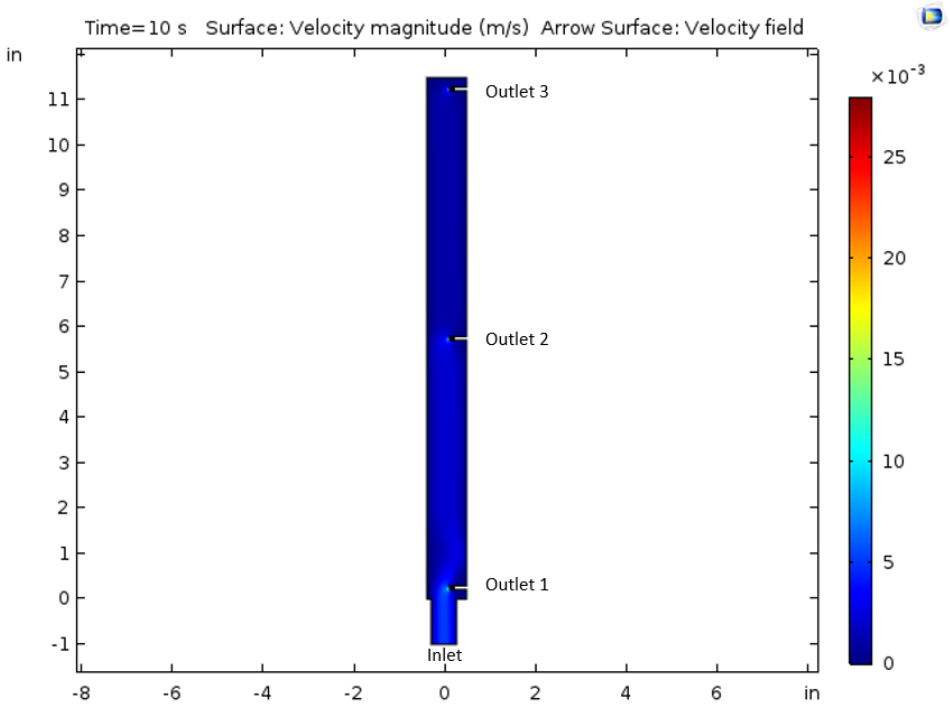

Figure 7. Velocity magnitude distribution for all channels inserted 9.525 mm (0.375 in) and a flowrate of 0.05 kg/s

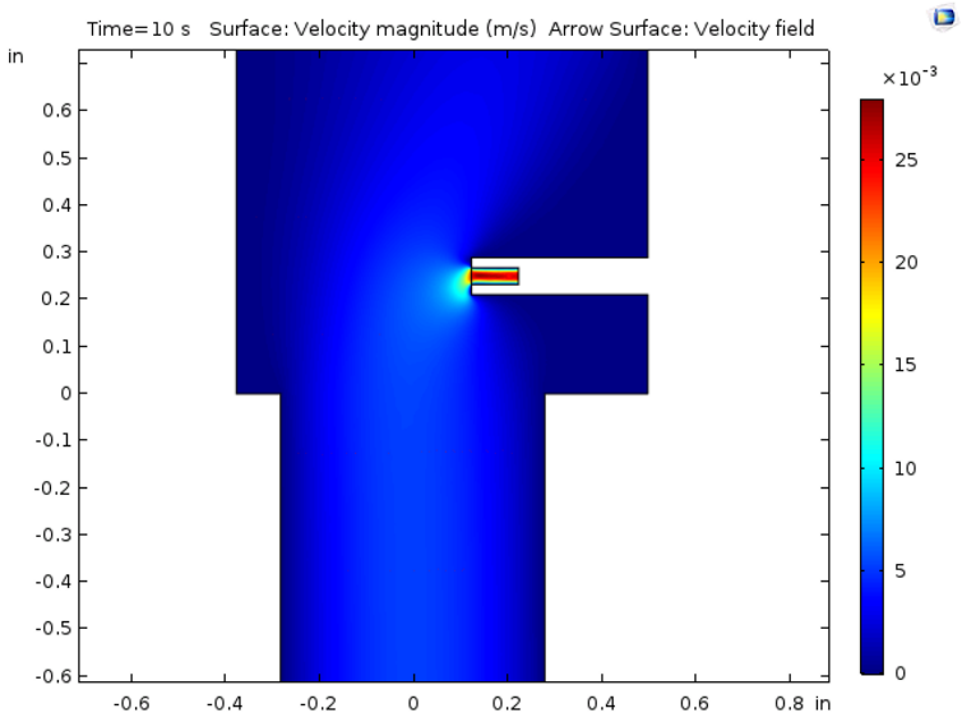

Figure 8. Detail view of first microchannel outlet velocity magnitude distribution

The following figures compile the results of the parametric study and extract some general trends. The outlet mass flux was evaluated using a line integral operation on the specified outlet boundary. The outlet distribution is defined as the outlet mass flux divided by the total mass flux to give a normalized fraction of the total flowrate. Figure 9 below shows the distribution of outlet flowrates vs. the total mass flowrate. The general trend shows that the flow distribution has greater variation at higher total mass flowrates, and for the given mass flowrates outlet 1 tends to have the lowest flowrate for given combinations of insertion depth.

Figures Figure 10-Figure 12 show the flow distribution for outlets 1, 2 and 3 (corresponding to Figure 7) compared to their insertion depth respectively. We can see general trends that as a microchannel is inserted deeper into the header, it generally impedes flow and lowers the mass flowrate for that microchannel. This trend is strongest for the microchannel closest to the header inlet, which can be explained in that the inserted microchannel blocks some of the inlet. Conversely, the microchannel closest to the outlet has very little variation with insertion depth due to being at the far end of the header.

While there may be some clear trends here with regards to insertion depth, the actual maldistribution is only about 1% for single phase flow. Since the liquid phase is essentially incompressible, we would not expect to see much maldistribution. This result coincides with literature reporting that refrigerant-side maldistribution is much less significant than air-side maldistribution. We would however expect a greater level of maldistribution in a two-phase flow which allows for instabilities and compressibility within the header. Various options for simulating two-phase flow are explored in the next section for eventual implementation into the complete model.

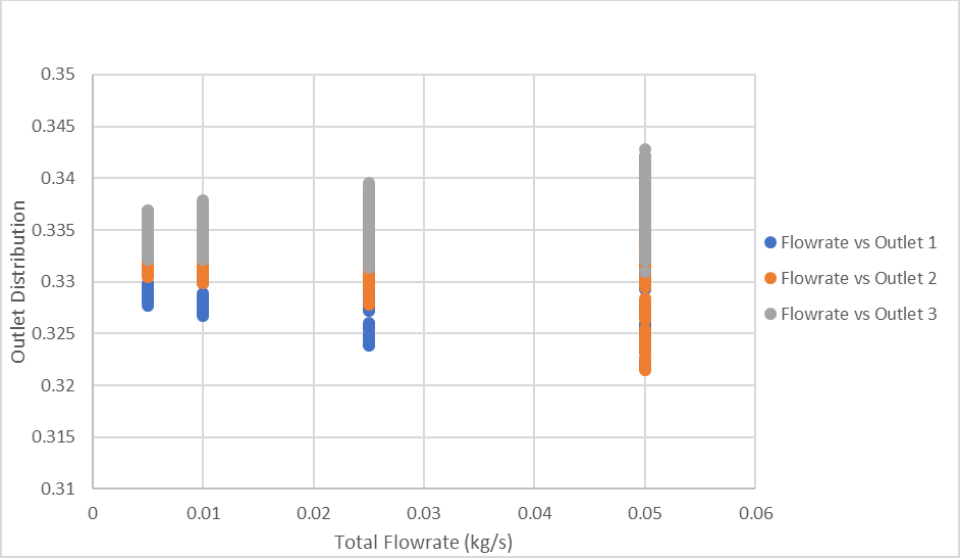

Figure 9. Total flowrate vs outlet distribution

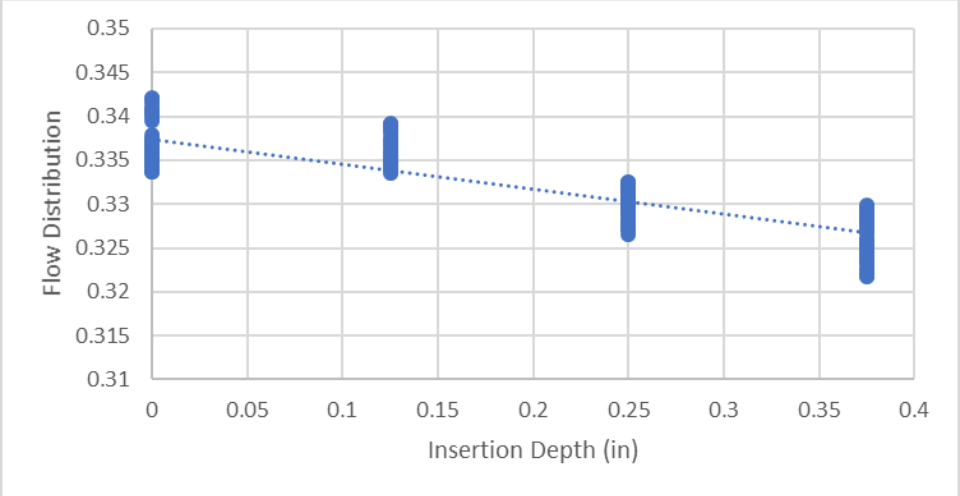

Figure 10. Outlet 1 insertion vs distribution

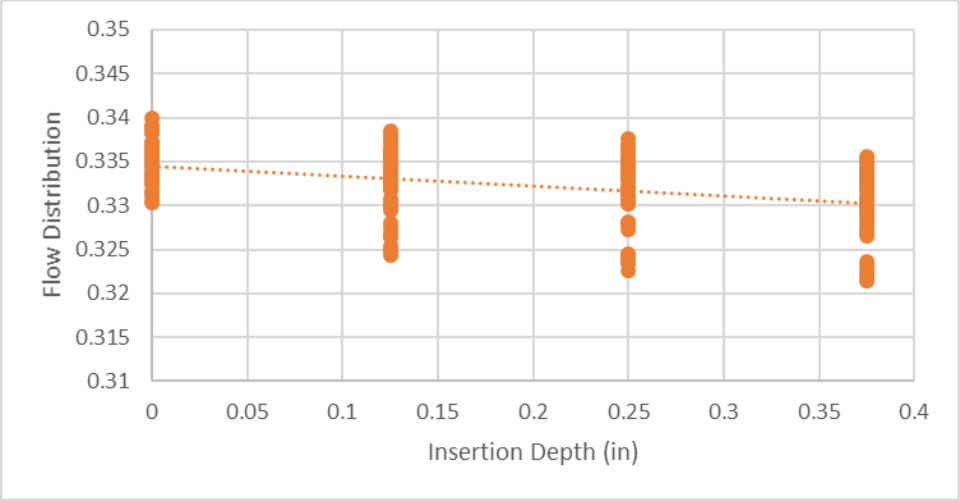

Figure 11. Outlet 2 insertion vs distribution

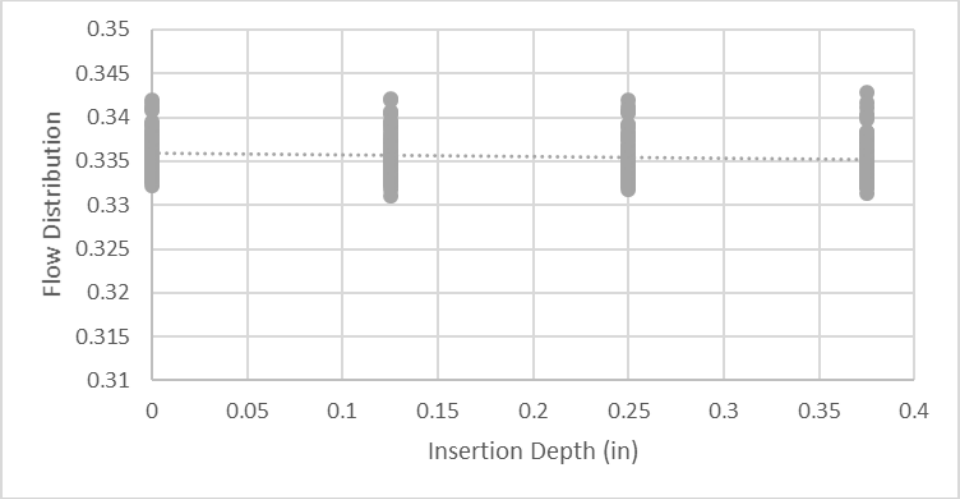

Figure 12. Outlet 3 insertion vs distribution

3. TWO-PHASE FLOW MODELING

COMSOL has a variety of interfaces available for simulating two-phase and multi-phase flows. Of those interfaces, there are two types of methods being bubbly flow and interface tracking. Bubbly flow allows for the tracking of a volume fraction of a gas phase as it disperses through a domain. It was briefly explored to see if gas phase might collect in some locations, but the presence of the gas phase does not influence the actual flow. For the interface tracking methods, COMSOL has modules for the level set method, phase field method, and moving mesh method. Of these three methods, moving mesh allows for the most accurate modeling of the shape of a liquid vapor interface, but such accuracy is not necessarily required. The level set and phase field methods are similar in that they use a phase function to track the interface. The level set method is purely mathematically based, and thus is less accurate physically. The phase field method is based on minimization of chemical potential, and thus is more accurate from a physics perspective. Both however have limitations in that the interface size is dependent on the mesh. These methods are also both computationally expensive, and so are explored preliminarily in 2D before eventual implementation into a fully coupled model.

Some preliminary results of the bubbly flow method are shown below in Figure 13. Here we can see approximately 5% gas by volume flowing into the header. As the gas propagation has no effect on the flow field, this method was quickly abandoned in favor of the interface tracking methods.

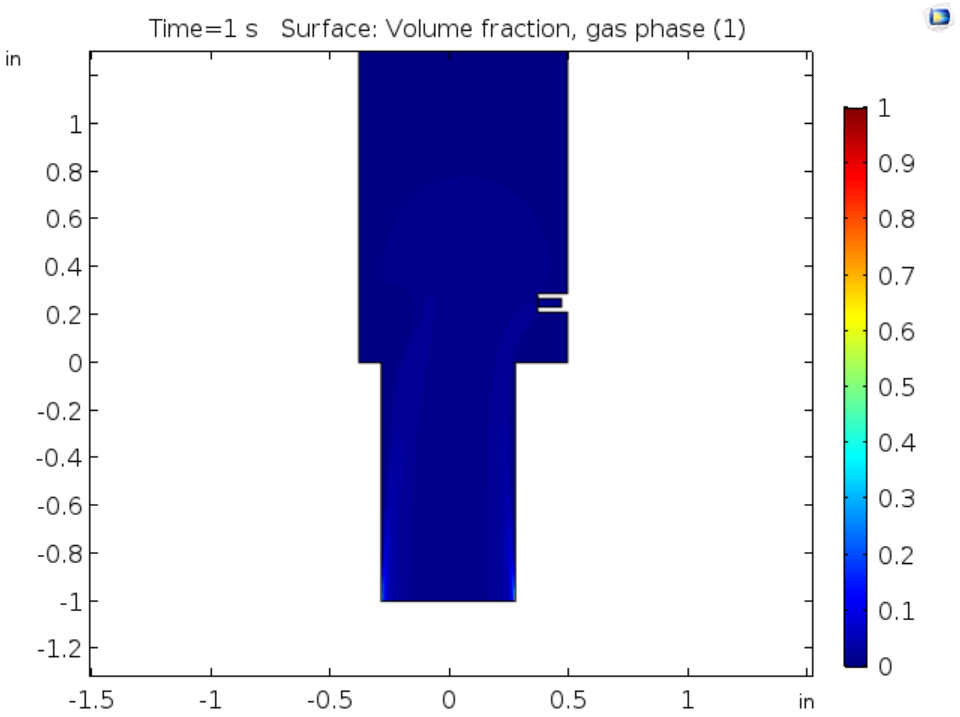

Figure 13. Preliminary results for bubbly flow method showing surface volume fraction of gas phase

3.1 PRELIMINARY RESULTS FROM THE LEVEL SET METHOD

The level set method is a method for numerical analysis of surfaces. It allows for easy modeling of shapes that change topology, for instance a bubble breaking apart. For CFD simulations, the level set function has a positive value for one phase, and a negative value for the other. The level set equation in nonconservative form as solved in COMSOL is shown in Eq. 6. The level set equation in conservative form is shown in Eq. 7. The nonconservative form is more numerically stable, but the overall mass of the

system is not explicitly conserved and can change due to numerical error propagating over time. The conservative form prevents that mass loss but makes the equation more difficult to solve and thus is avoided if the mass loss is negligible.

$$\frac{\partial \phi}{\partial t} + u \cdot \nabla \phi = \gamma \nabla \cdot \left(\epsilon_{ls} \nabla \phi - \phi(1-\phi) \frac{\nabla \phi}{|\nabla \phi|} \right) \tag{6}$$

$$\frac{\partial \phi}{\partial t} + \nabla \cdot (\mathrm{u}\phi) = \gamma \nabla \cdot \left(\epsilon_{ls} \nabla \phi - \phi(1-\phi) \frac{\nabla \phi}{|\nabla \phi|} \right) \tag{7}$$

In the above equations, ϕ is the level set variable which has a value of 1 for one phase, and a value of 0 for the other phase; γ is a reinitialization parameter that is left at the default value of 1 m/s; ϵ_{ls} is a parameter controlling the interface thickness and is dependent on the mesh. It is specified as a multiple of the average element size because the mesh must be uniform throughout the domain. Therefore, a finer mesh results in a thinner interface region. The level set variable varies smoothly across the interface, and the material parameters of density and viscosity are varied in the domain based on the value of ϕ shown in Eqs. 8 and 9, with the subscript denoting the material property of the phase corresponding with the level set variable specified.

$$\rho = \rho_1 + (\rho_2 - \rho_1)\phi \tag{8}$$

$$\mu = \mu_1 + (\mu_2 - \mu_1)\phi \tag{9}$$

Wetted wall boundary conditions replace the typical no-slip conditions from the laminar flow module. For this boundary condition, a contact angle, θ_w, and slip length, β, are specified. The contact angle was defined as $3\pi/8$ based on typical contact angles for air-water. The slip length is defined automatically by COMSOL and is dependent on the mesh size. The wetted wall boundary conditions are shown in Eqs. 10-12.

$$n \cdot u = 0 \tag{10}$$

$$-\nabla \cdot N_\phi = 0 \tag{11}$$

$$F_{wall} = \sigma(n - n_{int}\cos\theta_w)\delta - \frac{\mu}{\beta}u \tag{12}$$

For the present simulations, a region of the domain is defined as liquid water while another region is defined as air. Typical simulations involved the movement of an air bubble in a channel, or movement of an air slug in a microchannel shown in Figure 14. Simulations are carried out in 2D geometry due to the computational expense of the interface tracking methods. In addition to the time-dependent study, a phase initialization step must occur prior to solving to resolve the initial interfaces. The bubble simulations were eventually implemented into the same 2D header geometry as the benchtop experiment; however, these models do not account for the effect of gravity collecting bubbles on the top surface of the header.

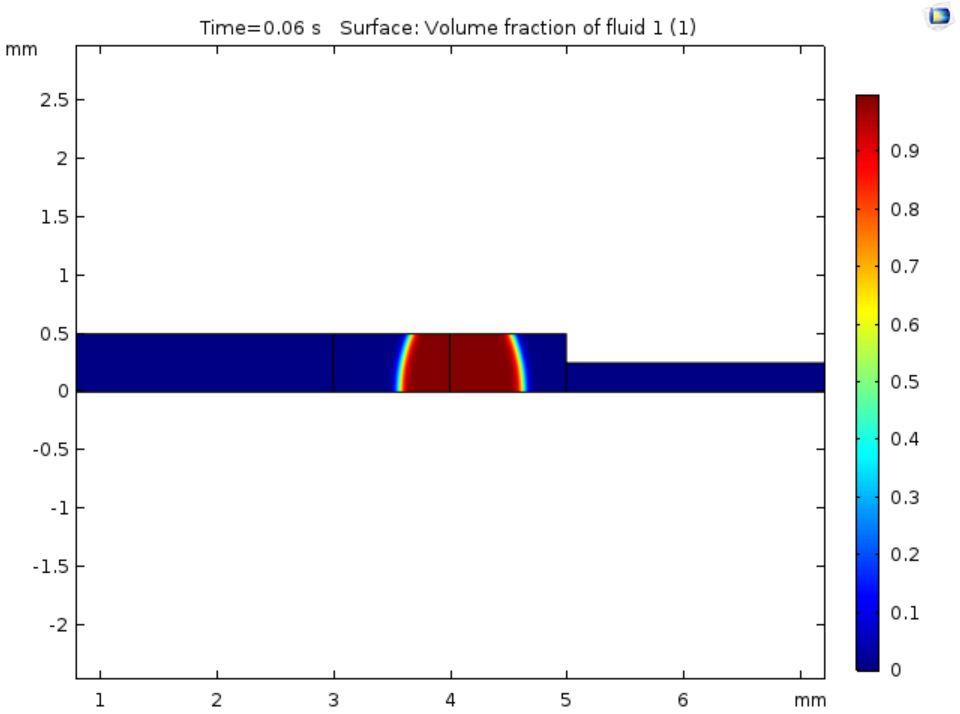

Figure 14. Air slug flow in a 2D converging microchannel using level set method

3.2 PRELIMINARY RESULTS FROM THE PHASE FIELD METHOD

The phase field method is governed by the Cahn-Hilliard equation which tracks the diffuse interface between two immiscible fluids. The phase field method is similar to the level set method in that there is a phase field parameter advected by the velocity from Navier-Stokes. However, that phase field parameter is influenced by a free energy function derived from statistical physics. There are still parameters regarding the interface width, which is necessary due to the discretization of the numerical domain. The phase field equations in nonconservative form as solved by COMSOL are shown in Eqs. 13-16. The phase field method is vulnerable to the same mass loss due to numerical error as the level set method, and thus as required there is a similar conservative form shown in Eq. 17.

$$\frac{\partial \phi}{\partial t} + u \cdot \nabla \phi = \nabla \cdot \frac{\gamma \lambda}{\epsilon_{pf}^2} \nabla \psi \tag{13}$$

$$\psi = -\nabla \cdot \epsilon_{pf}^2 \nabla \phi + (\phi^2 - 1)\phi + \frac{\epsilon_{pf}^2 \partial f}{\lambda \, \partial \phi} \tag{14}$$

$$\lambda = \frac{3\epsilon_{pf}\sigma}{\sqrt{8}} \tag{15}$$

$$\gamma = \chi \epsilon_{pf}^2 \tag{16}$$

$$\frac{\partial \phi}{\partial t} + \nabla \cdot (\mathrm{u}\phi) = \nabla \cdot \frac{\gamma \lambda}{\epsilon_{pf}^2} \nabla \psi \tag{17}$$

The phase field having two equations to define the interface makes the simulation more computationally expensive, but it is generally more accurate than the level set method because of its grounding in physics. The variable λ is the mixing energy density and ϵ_{pf} is the interface thickness parameter based on the mesh. The variable ψ is known as the phase field help variable and σ is the surface tension coefficient. The material properties are evaluated similarly to the level set method, except that ϕ varies between -1 and 1. Thus, the volume fraction of each fluid must be defined as shown in Eqs. 18 and 19.

$$V_1 = \frac{1-\phi}{2} \tag{18}$$

$$V_2 = \frac{1+\phi}{2} \tag{19}$$

Thus, the material properties for the level set method are evaluated as shown in Eqs. 20 and 21.

$$\rho = \rho_2 + (\rho_1 - \rho_2)V_1 \tag{20}$$

$$\mu = \mu_2 + (\mu_1 - \mu_2)V_1 \tag{21}$$

All walls of the geometry are defined as wetted walls with a contact angle θ_w of 3π/8 as shown in Eqs. 22 and 23.

$$n \cdot \frac{\gamma\lambda}{\epsilon_{pf}^2}\nabla\psi = 0 \tag{22}$$

$$n \cdot \epsilon_{pf}^2\nabla\phi = \epsilon_{pf}^2 \cos\theta_w|\nabla\phi| \tag{23}$$

Similar to the level set method, a phase initialization step is required to resolve the interface between the two fluid domains. A uniform density mesh is also required to properly map the travel of the interface in the case of a moving bubble. If the interface is somewhat localized though, the mesh far from the interface need not be constrained. Because two-phase flow is being approximated with air-water mixtures in the concurrent benchtop experiment, air and water were also used for the simulations.

Simple cases of an air bubble in a channel were explored initially. The purpose of these simplified cases was to gain an understanding of these two-phase modeling techniques so they could be applied to a larger complex model. The phase field after the phase initialization step is shown in Figure 15. Note the interface region is relatively thick corresponding to a coarse mesh as shown. A similar case of a bubble in a corner channel is shown in Figure 16. Laminar flow boundary conditions are similar to the single-phase simulations. The walls are specified as no-slip. The outlet is specified to have a pressure of 0 Pa gauge. The inlet in this case was specified to have an average velocity of 0.02 m/s. While these cases may be simple, a fine mesh is required to properly capture the physics, and thus time steps are typically very small. Simulating the motion of a bubble on a larger time scale thus takes a substantial amount of time, even in 2D.

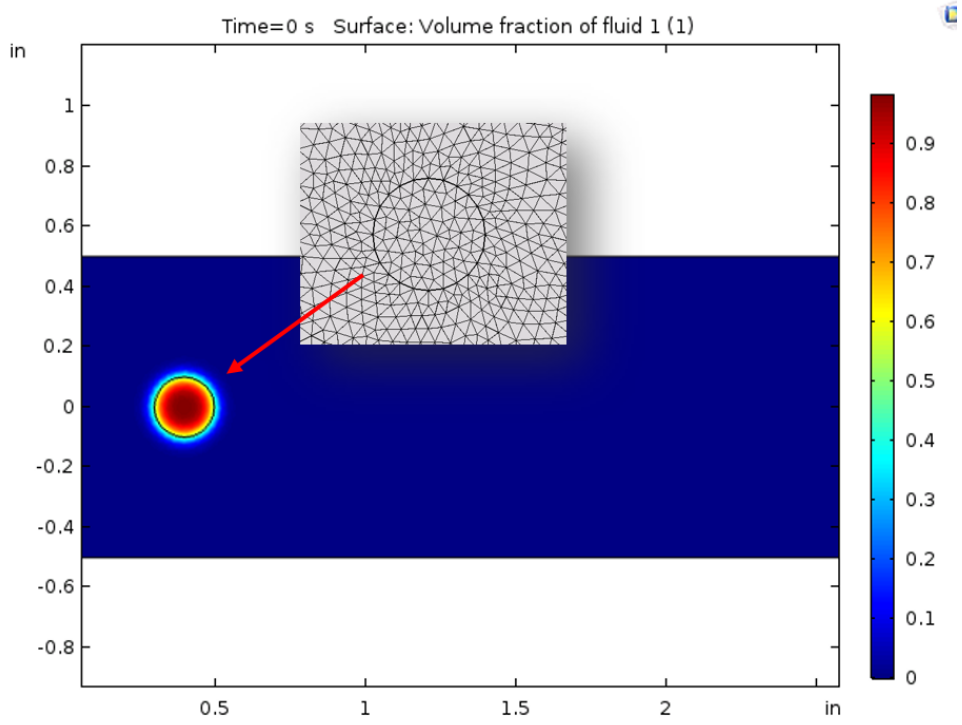

Figure 15. Air bubble in water channel simulated with phase field method

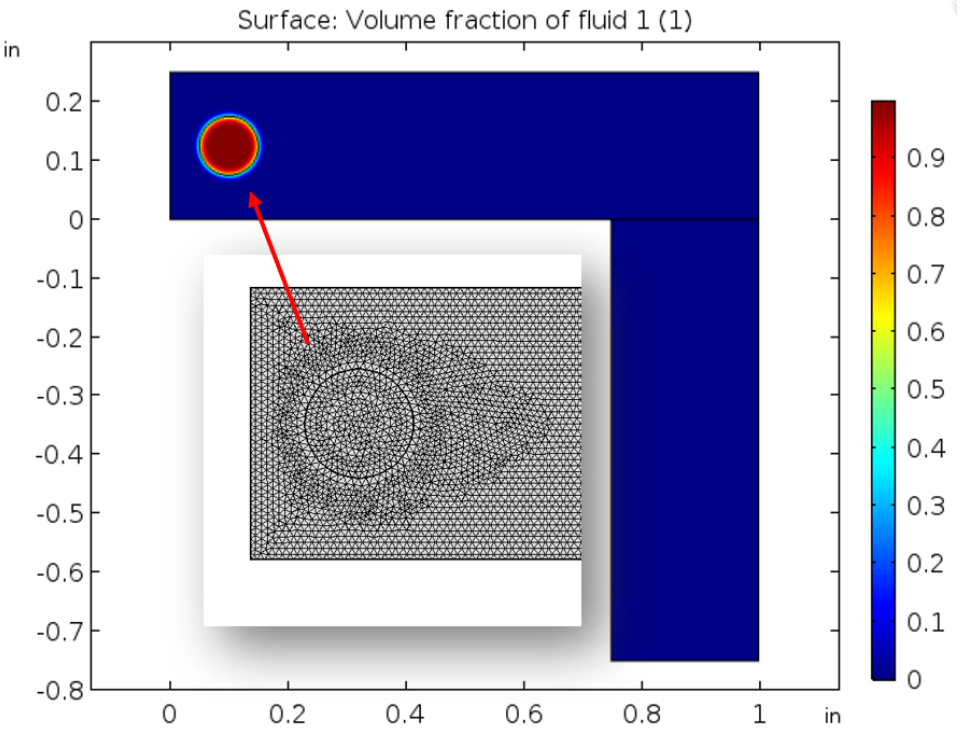

Figure 16. Air bubble in a corner channel simulated with phase field method

3.3 APPLICATION OF TWO-PHASE FLOW MODELS TO HX HEADER GEOMETRY

Applying the level set and phase field methods to the 2D header geometry, we can begin to see the effect of two-phase flow on maldistribution. In one model, an air pocket was added to the end of the header. The inlet of the header is specified as a mass flow rate of water, with the outlets at atmospheric pressure. The interface near the header is shown below in Figure 17. Note that the air pocket undulates over time as the model approaches a steady state. The evolution of the air pocket interface is shown in Figure 18. For a total mass flowrate of 0.14 kg/s we can see the flow distribution in each of the header outlets in Figure 19.

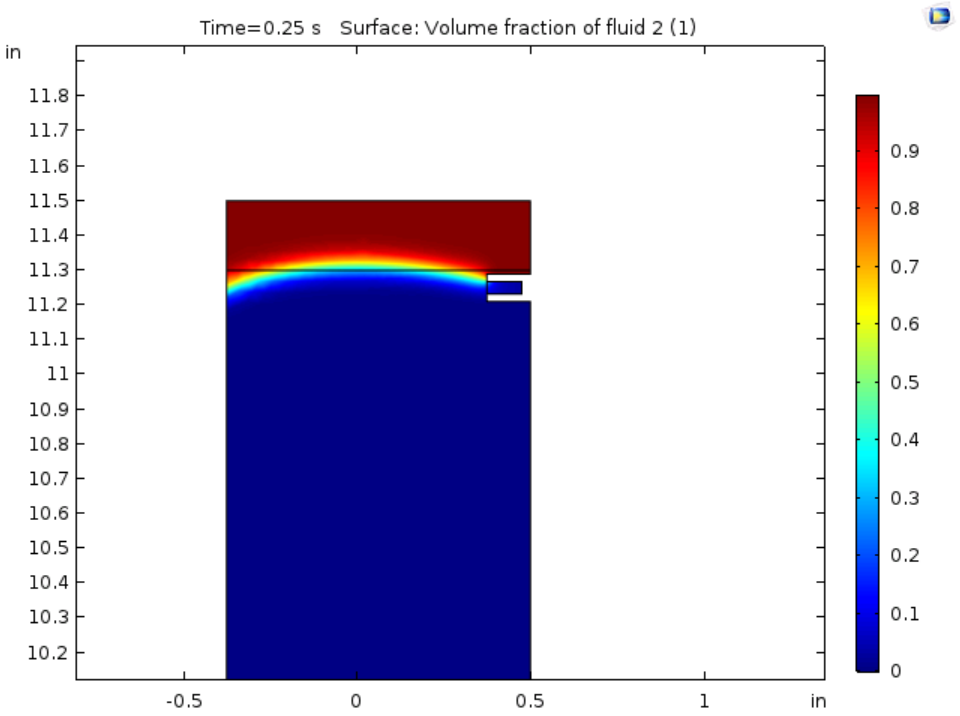

Figure 17. Air pocket at the end of header geometry using conservative phase field method

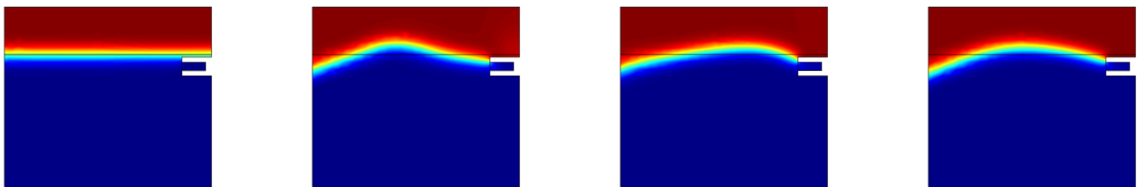

(a.) (b.) (c.) (d.)

Figure 18. Interface motion at various times (a) 0 s, (b) 0.05 s, (c) 0.1 s, (d) 0.15 s

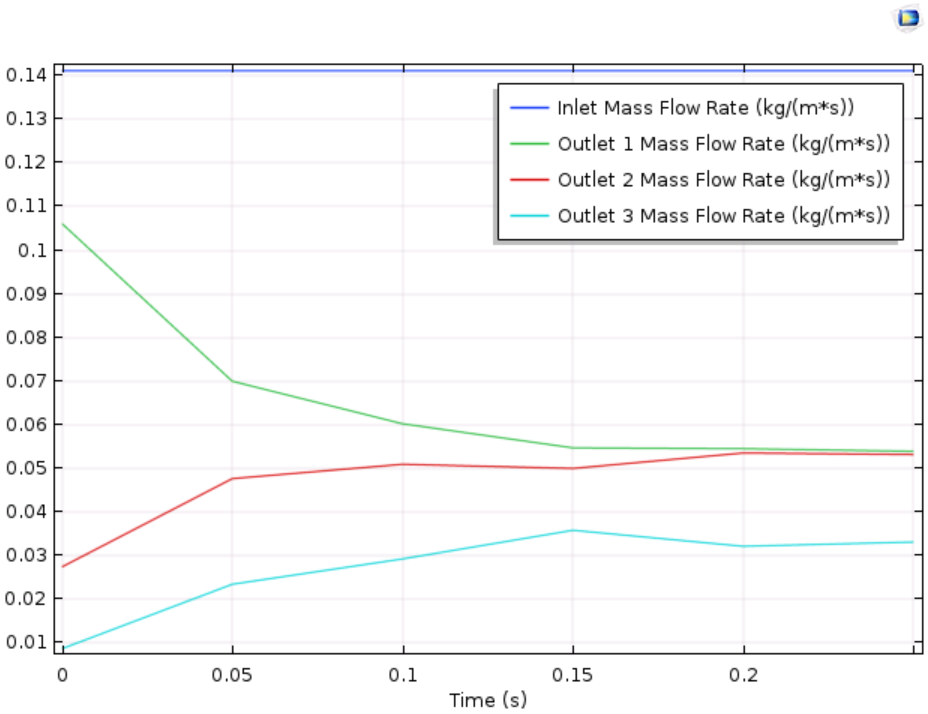

Figure 19. Mass flowrates for air pocket model using phase field method

With the presence of an air pocket, we can see that the mass flowrate for outlet three is substantially lower than the other two outlets as steady state is approached. This is showing that the air proximity to the outlet has an effect, either through obstructing the flow or altering the flow field near the inlet. The velocity vectors are shown as arrows in Figure 20. This result is consistent with the benchtop experimental results. In the benchtop experiment, the air bubbles entering the header rise to the top due to gravity, but first collect near outlet 1. The collection of air near the outlet substantially reduced the flow. The 2D model is unable to account for the gravity effect in the horizontal header, but a similar effect is observed near the imposed air pocket. To showcase the difference between conservative and nonconservative equation forms, Figure 21 shows the growth of the air pocket when using the nonconservative level set method. Given enough time for numerical errors to propagate, the total volume of air noticeably increases. Thus, to maintain solution accuracy, the conservative method is required for future models.

These methods were explored and shown to be able to accurately model the influence of a liquid vapor interface on fluid flow. Such a model will be implemented into a future complex model also encompassing ultrasound driven fluid motion. The two-phase flow will likely have a substantial effect on the ultrasound wave propagation, as air bubbles tend to reflect sound waves and could potentially interrupt any acoustic streaming phenomenon.

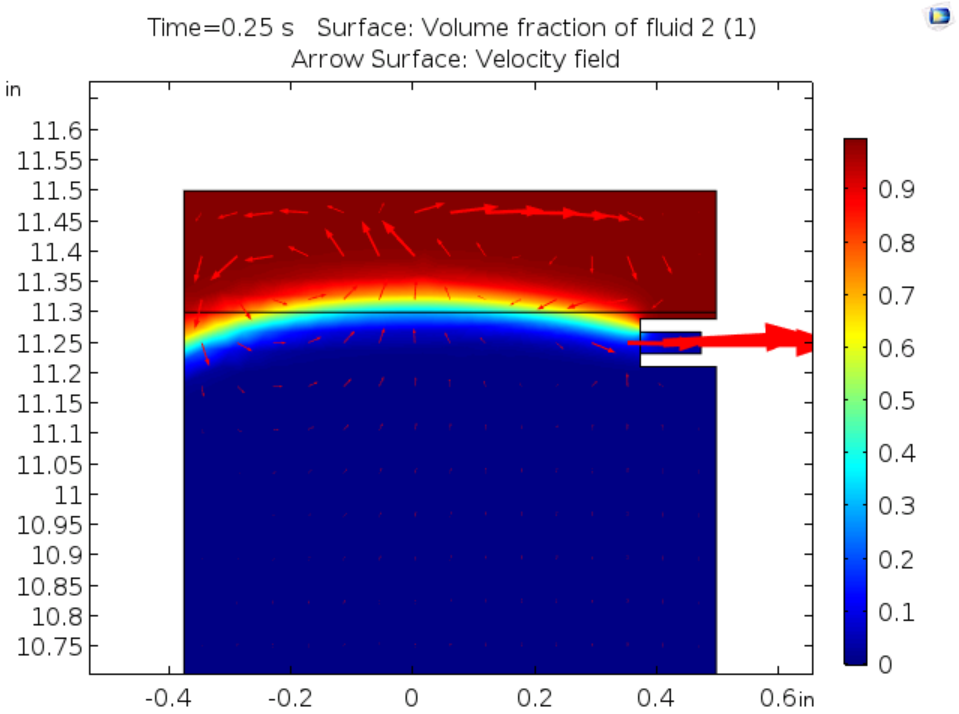

Figure 20. Velocity vectors by air pocket with phase field method

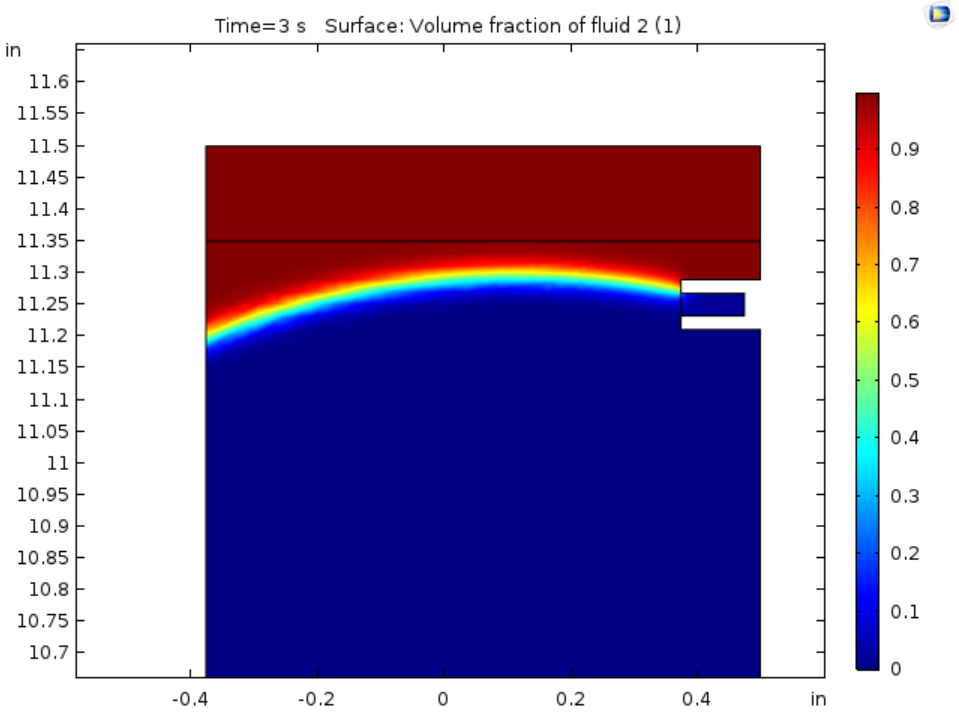

Figure 21. Air pocket growth from nonconservative level set method.

4. ULTRASOUND MODELING

The goal of ultrasound modeling is to gain some fundamental understanding about how to influence the fluid flow field using piezoelectric transducers. Specifically, these models aim to explore the effect of acoustic streaming phenomenon, which is the result of the attenuation of sound waves in the fluid. There are two methods we are currently exploring. The first method involves direct simulation of a vibrating surface interacting with a fluid. The second method involves decoupling the acoustics from the fluid flow and evaluating a body force term based on the acoustic pressure field. Efforts have primarily been focused on the first method thus far.

COMSOL's acoustic interfaces are designed to reduce the computational cost of analysis. The built in acoustic and ultrasound interfaces are able to model the propagation of waves through a background flow, but it is a one-way coupling. In other words, the flow influences the acoustics, but the acoustics do not influence the flow. Therefore, it is required we model using the more computationally expensive approach through the fluid-structure interaction module.

The fluid-structure interaction module employs the Arbitrary LaGrangian-Eulerian (ALE) method. Because the solid mechanics and fluid mechanics equations are formulated differently, this method can bridge them using a moving mesh technique. This is somewhat computationally expensive, as the mesh is reevaluated at every time step. The governing equations for each interface remain the same (See Eqs 1-5 for the laminar flow interface). The solid mechanics interface equations assume a linear elastic material. Linear elastic materials are governed by three equations: the equation of motion, the strain displacement equation, and a constitutive equation (Hooke's law) as shown in equations Eqs. 24-26, respectively. Additional equations as defined by the COMSOL interface are shown in Eqs. 27-31.

$$\rho\frac{\partial^2 u_{solid}}{\partial t^2} = \nabla \cdot (FS)^T + F_v \tag{24}$$

$$\varepsilon = \frac{1}{2}\left[(\nabla u_{solid})^T + \nabla u_{solid} + (\nabla u_{solid})^T \nabla u_{solid}\right] \tag{25}$$

$$C = C(E,\nu) \tag{26}$$

$$F = I + \nabla u_{solid} \tag{27}$$

$$S = S_{ad} + JiF_{inel}^{T}(C{:}\varepsilon_{el})F_{inel}^{-1} \tag{28}$$

$$\varepsilon_{el} = \frac{1}{2}\left(F_{el}^{T}F_{el} - I\right) \tag{29}$$

$$F_{el} = FF_{inel}^{-1} \tag{30}$$

$$S_{ad} = S_0 + S_{ext} + S_q \tag{31}$$

In this notation, $(C{:}\varepsilon_{el})$ is the Cauchy stress tensor nd C is the stiffness tensor which is a function of Young's modulus and Poisson's ratio; F_v is the body force per unit volume; S represents the Second Piola-Kirchoff stress. For the present model, vibration of a solid body exposed to the fluid domain is imposed by a boundary load on one side. The boundary load is defined in Eq. 32.

$$S \cdot \mathrm{n} = F_A \tag{32}$$

The force is also applied as a distribution in the r-direction, such that maximum force is applied at the center of the transducer, and no force is applied at the edge. A sine wave function with angular frequency $2\pi f_0$ defines the cyclic loading to vibrate the surface, where f_0 is the applied frequency. The applied force boundary condition value is shown in Eq. 33.

$$F_{applied} \sin\left(2\pi f_0\right)(10 - r) \tag{33}$$

The side of the transducer is left as a free surface. The boundary at r = 0 is a symmetry condition. The bottom boundary of the solid is defined as either fixed or a roller boundary condition shown in Eqs. 34 and 35, respectively.

$$u_{solid} = 0 \tag{34}$$

$$n \cdot u_{solid} = 0 \tag{35}$$

The model is set up as a 2D axisymmetric geometry replicating a vibrating cylindrical transducer of radius 10 mm and height 5 mm. The cylindrical fluid domain has a radius of 30 mm and a height of 50 mm. The blue region denotes the fluid domain in Figure 22, while the grey region is the solid domain. The right and top boundaries of the fluid domain are open, while the bottom and transducer surface are no-slip. The domain is partitioned such that fine meshing can done near the transducer, while a mapped mesh can be used in the far field regions. An extremely fine mesh is required near the transducer to properly capture the high velocity gradients as vibration occurs. The mesh quality plot is shown in Figure 23.

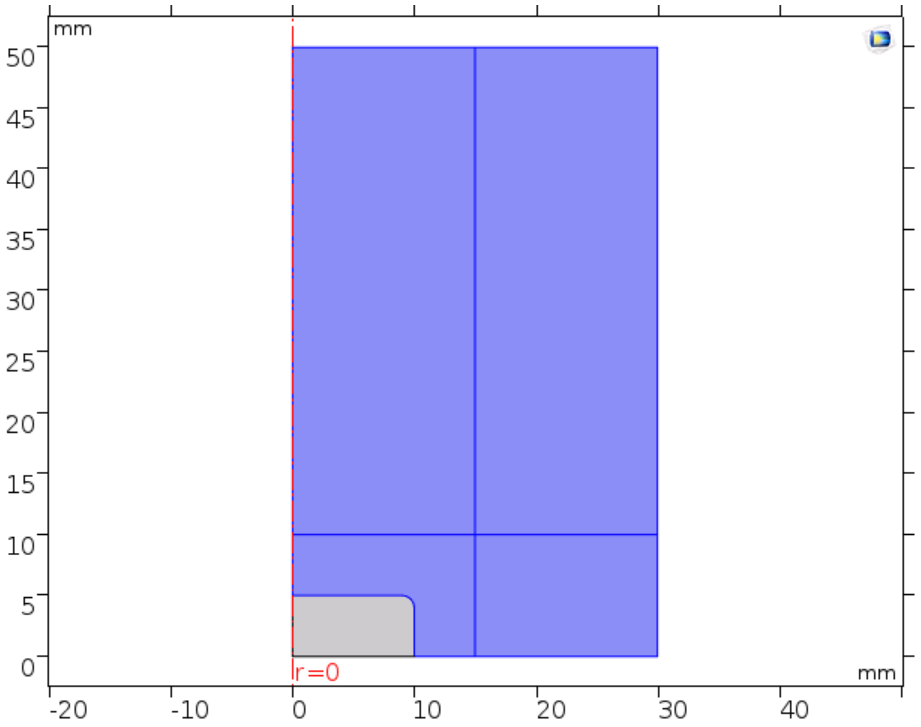

Figure 22. Fluid-structure interaction model domain

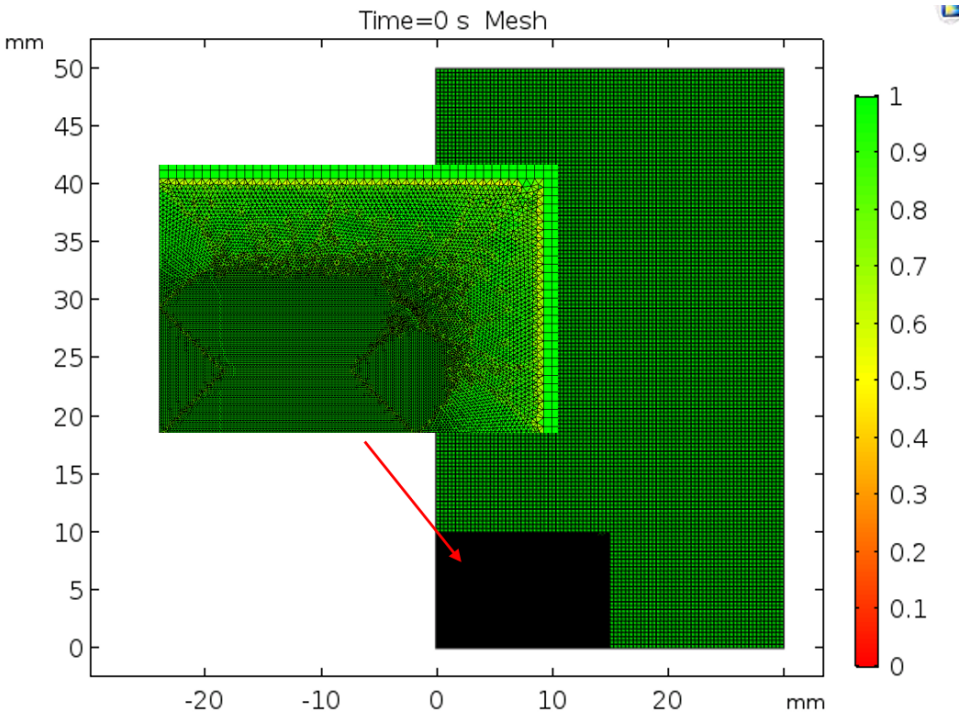

Figure 23. Mesh quality plot with detailed view for fluid-structure interaction model

Results from this model appear promising. For a given vibrational frequency, if a substantial enough displacement occurs, a jet is produced. The acoustic streaming jet is formed by the attenuation of pressure waves in the fluid over a long enough time scale. An important result of this modeling is that we can see the approximate time scale required for a vibrating piezo to produce bulk fluid motion, which is on the order of several milliseconds. For a lower frequency, a higher displacement is required to create the fluid jet phenomenon. Essentially there is a minimum amount of energy that the vibrating surface must transmit into the fluid for the phenomenon to occur. Figure 24 shows a comparison of the results for various frequencies, applied forces, and times. For the same applied force and time, a higher frequency produces a faster jet. If the frequency is too low for a given displacement as in case (e.), a jet will not form at all. Similarly, if the applied force is too low for a given frequency as in case (d.), a jet will not form either. In case (f.), a jet is still able to form at 5 kHz if the applied force is increased.

This modeling approach has proven to be successful at translating vibration from a surface into fluid motion. The accuracy of such method needs to be verified experimentally, but still gives good insight into the underlying phenomenon. There is clearly a trade-off between the energy exerted by the transducer and the bulk fluid motion created. It will be important to determine whether the benefits provided by the bulk fluid motion to combat maldistribution outweigh the energy cost to induce that motion.

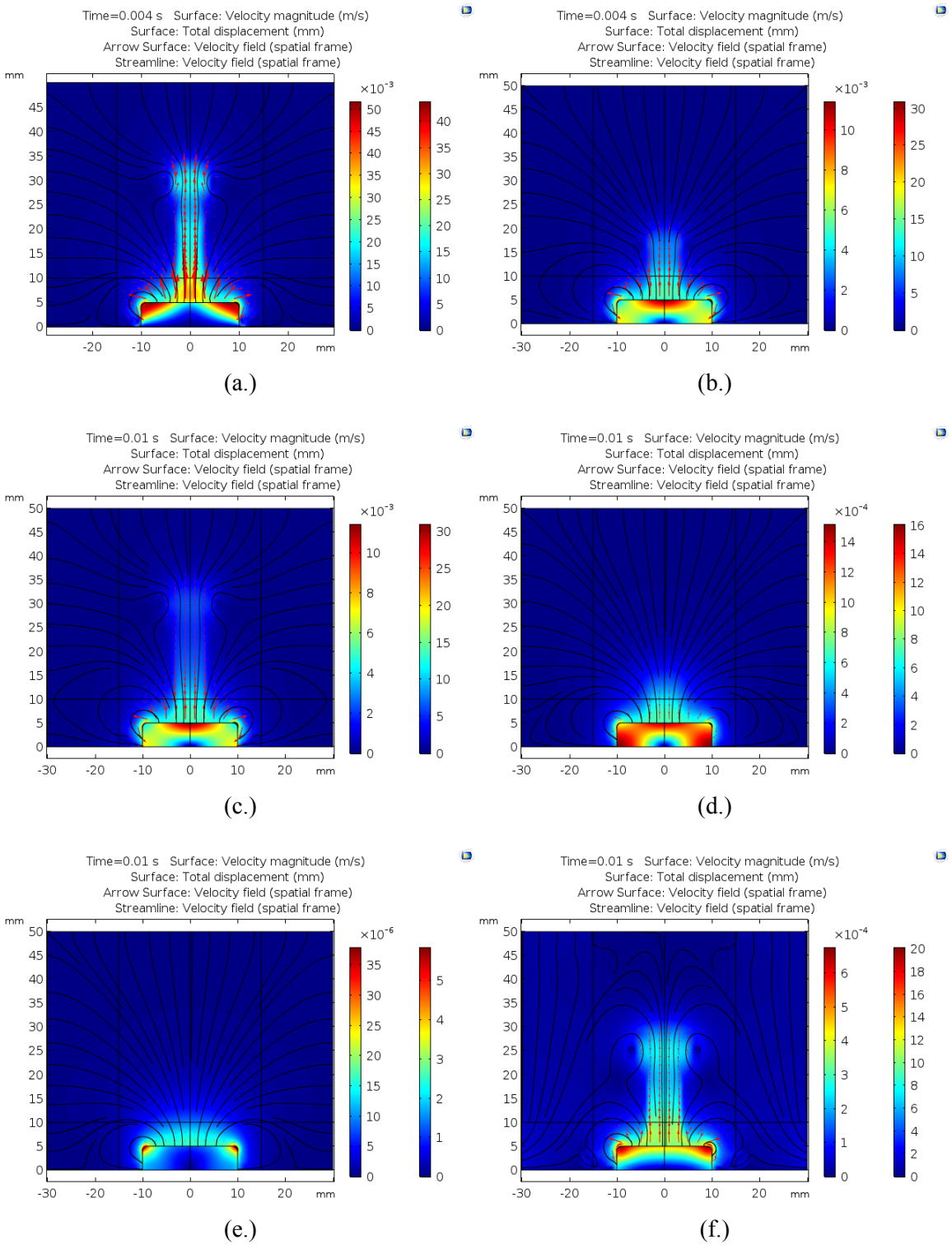

Figure 24. Comparison of results for various frequencies, applied forces, and times: (a.) 25 kHz, 5×10^6 N/m^3, 0.004 s; (b.) 20 kHz, 5×10^6 N/m^3, 0.004 s; (c.) 20 kHz, 5×10^6 N/m^3, 0.01 s; (d.) 20 kHz, 2.5×10^6 N/m^3, 0.01 s; (e.) 5 kHz, 5×10^6 N/m^3, 0.01 s; (F) 5 kHz, 2×10^7 N/m^3, 0.01 s.

The above fluid-structure interaction simulations have one major disadvantage in that they are computationally expensive. Specifically, in solving fully coupled structure and fluids equations, as well as the ALE method requiring remeshing of the entire domain at every time step. In order to properly capture the motion of the transducer, it is also required to have multiple time steps during each oscillation of the surface. Because of this, the time step size decreases for increasing frequency. Increasing the frequency any substantial amount will make the computation prohibitively expensive, especially when implemented into the larger header domain. Therefore, we are limited to only simulating lower frequencies. It is also important to note that simulation time will increase drastically in a full 3D geometry compared to 2D axisymmetric.

The other approach for modeling the acoustic streaming effect is based on classical theory developed by Gusev and Rudenko [3] and has an advantage over the fluid-structure interaction method in that it is less computationally expensive. The method decouples the high frequency acoustics from the fluid flow. A body force term is added to fluid momentum equation that accounts for time-averaged acoustic pressure, density variation, and velocity [4]. This allows for the problem to be solved in steady state, which also reduces error propagation from time derivatives. This method has been applied successfully in recent work with modeling of liquid metal processing but relies on simplifications [5,6]. The force term is shown in Eq. 36 below

$$F = -\frac{1}{2}\nabla\overline{v_a \cdot v_a} - \frac{c_0^2}{2\rho_0^2}\left[\frac{\rho_0}{c_0^2}\left(\frac{\partial^2 p}{\partial \rho^2}\right)_{\rho=\rho_0} - 1\right]\nabla\overline{\rho_a^2} - \frac{1}{\rho_0^2}\left(\zeta + \frac{\mu}{3}\right)\nabla\nabla\cdot\overline{(\rho_a v_a)} - \frac{\mu}{\rho_0^2}\overline{\rho_a\nabla^2 v_a} \quad (36)$$

where v_a is the acoustic velocity and p is the pressure in the fluid domain, which oscillates due to the ultrasound waves; c_0 is the speed of sound and ρ_0 is the density of the fluid, which is assumed constant on the low frequency time scale; ρ_a is the density perturbation due to the ultrasound pressure wave, ζ is the fluid's bulk viscosity, and μ is the fluid's dynamic viscosity. Overbars are time-averaged terms obtained in the frequency domain. It is important to note in this force term that fluid viscosity is inherently required to produce a net force, as this is the method through which ultrasound energy is transferred into fluid momentum.

This method first solves the pressure acoustics in COMSOL through the Helmholtz equation with an attenuation term in the frequency domain. Then the body force term described above can be evaluated, and the fluid equations can be solved. This force term make convergence particularly difficult though, and techniques such as force ramping are required. In addition, the fluid flow is assumed laminar for the sake of convergence even though the flow is turbulent in close proximity to the pressure source. Because of this assumption, the magnitude of the solution can be off, but the approximate "shape" of the flow field can be predicted accurately as shown in Rubinetti et al. [5]. This method was briefly explored, but it was decided to focus on the acoustic-structure interaction method.

5. CONCLUSIONS

A compartmental approach to modeling our desired system allows for the gradual introduction of complexity and the ability to understand the fundamentals of the modeling methods and phenomenon. Having shown no appreciable maldistribution in single-phase as expected, two-phase flow and acoustic interactions were explored. Two-phase models utilizing the level set and phase field methods are able to show maldistribution in the presence of air bubbles in water. Fluid-structure interaction allows for the modeling of the acoustic streaming phenomenon which may be used to influence the flow. Even more complex interactions will be introduced as the acoustics begin to interact with two-phase flow. Additionally, we will explore the use of the acoustic streaming phenomenon to attempt to rebalance flow given an artificially introduced maldistribution via upstream pressure boundary conditions. The modeling effort will continue as the project progresses. Valuable insight gained from the numerical models will aid in the design of the benchtop experiment going forward.

6. REFERENCES

[1] COMSOL Inc., 2019, COMSOL Multiphysics 5.3, Stockholm, Sweden

[2] Kim, J., Braun, J., & Groll, E. (2009). Evaluation of a hybrid method for refrigerant flow balancing in multi-circuit evaporators. International Journal of Refrigeration, 32(6), 1283–1292. https://doi.org/10.1016/j.ijrefrig.2009.01.016

[3] V. E. Gusev and O. V. Rudenko, "Nonstready quasi-one-dimensional acoustic streaming in unbounded volumes with hydrodynamic nonlinearity," Sov. Phys. Acoust. 25, 493-497 (1979).

[4] Kamakura, T., Matsuda, K., Kumamoto, Y., & Breazeale, M. (1995). Acoustic streaming induced in focused Gaussian beams. The Journal of the Acoustical Society of America, 97(5), 2740–2746. https://doi.org/10.1121/1.411904

[5] Rubinetti, D., Weiss, D., Muller, J., Wahlen, A. (2016). Numerical modeling and validation concept for acoustic streaming induced by ultrasonic treatment. COMSOL Conference 2016 Munich. Retrieved from: https://www.comsol.com/paper/numerical-modeling-and-verification of-acoustic-streaming-induced-by-ultrasonic--38061

[6] Rubinetti, D., Weiss, D. Ultrasound-Driven Fluid Motion - Modelling Approach. (2018). The International Journal of Multiphysics, 12(1). https://doi.org/10.21152/1750-9548.12.1.1